

The Three Hundred project: Estimating the dependence of gas filaments on the mass of galaxy clusters

Sara Santoni^{1,2,3}, Marco De Petris¹, Gustavo Yepes^{2,4}, Antonio Ferragamo¹, Matteo Bianconi⁵, Meghan E. Gray⁵, Ulrike Kuchner⁵, Frazer R. Pearce⁵, Weiguang Cui^{2,4,6}, and Stefano Ettori^{7,8}

¹ Dipartimento di Fisica, Sapienza Università di Roma, Piazzale Aldo Moro 5, I-00185 Rome, Italy
e-mail: sara.santoni@uniroma1.it

² Departamento de Física Teórica, Facultad de Ciencias, Universidad Autónoma de Madrid, Modulo 8, E-28049 Madrid, Spain

³ Escuela de Doctorado UAM, Centro de Estudios de Posgrado, Universidad Autónoma de Madrid, E-28049, Madrid, Spain

⁴ Centro de Investigación Avanzada en Física Fundamental (CIAFF), Facultad de Ciencias, Universidad Autónoma de Madrid, E-28049, Madrid, Spain

⁵ School of Physics and Astronomy, University of Nottingham, Nottingham NG7 2RD, UK

⁶ Institute for Astronomy, University of Edinburgh, Edinburgh EH9 3HJ, UK

⁷ INAF, Osservatorio di Astrofisica e Scienza dello Spazio, via Piero Gobetti 93/3, I-40129 Bologna, Italy

⁸ INFN, Sezione di Bologna, viale Berti Pichat 6/2, I-40127 Bologna, Italy

Received ...; accepted ...

ABSTRACT

Context. Galaxy clusters are located in the densest areas of the universe and are intricately connected to larger structures through the filamentary network of the Cosmic Web. In this scenario, matter flows from areas of lower density to higher density. As a result, the properties of galaxy clusters are deeply influenced by the filaments that are attached to them, which are quantified by a parameter known as connectivity.

Aims. We explore the dependence of gas-traced filaments connected to galaxy clusters on the mass and dynamical state of the cluster. Moreover, we evaluate the effectiveness of the cosmic web extraction procedure from the gas density maps of simulated cluster regions.

Methods. Using the DisPerSE cosmic web finder, we identify filamentary structures from 3D gas particle distribution in 324 simulated regions of $30 h^{-1}$ Mpc side from THE THREE HUNDRED hydrodynamical simulation at redshifts $z=0, 1$, and 2 . We estimate the connectivity at various apertures for ~ 3000 groups and clusters spanning a mass range from $10^{13} h^{-1} M_{\odot}$ to $10^{15} h^{-1} M_{\odot}$. Relationships between connectivity and cluster properties like radius, mass, dynamical state and hydrostatic mass bias are explored.

Results. We show that the connectivity is strongly correlated with the mass of galaxy clusters, with more massive clusters being on average more connected. This finding aligns with previous studies in literature, both from observational and simulated data sets. Additionally, we observe a dependence of the connectivity on the aperture at which it is estimated. We find that connectivity decreases with cosmic time, while no dependencies on the dynamical state and hydrostatic mass bias of the cluster are found. Lastly, we observe a significant agreement between the connectivity measured from gas-traced and mock-galaxies-traced filaments in the simulation.

Key words. large-scale structure of Universe – Galaxies: clusters: general – Methods: numerical – Methods: statistical

1. Introduction

Clusters of galaxies, considered the largest gravitationally-bound structures in the universe, are located at the nodes of an intricate web-like structure known as the *Cosmic Web* (Bond et al. 1996). This cosmic pattern of dark matter (DM) and baryons and the formation of large-scale structures are predicted as a consequence of the non-linear growth of primordial density perturbations (Zel'dovich 1970; Peebles 1980). In this framework, matter flows from underdense regions to overdense structures, resulting in compact galaxy clusters at the nodes of elongated filamentary structures and filaments at the intersection of sheet-like formations, known as walls, surrounded by vast void regions.

The cosmic web has been observed by several galaxy surveys, such as the Sloan Digital Sky Survey (SDSS, York et al. 2000) and the 2dF Galaxy Redshift Survey (2dFGRS, Colless et al. 2001). Furthermore, the properties of the cosmic web and its components have been identified through several large-scale numerical simulations, both N-body and hydrodynamical, such

as the Millennium simulation (Springel 2005) and the MillenniumTNG project (Hernández-Aguayo et al. 2023), The Illustris project (Vogelsberger et al. 2014) and IllustrisTNG (Nelson et al. 2019), the EAGLE project (Schaye et al. 2015) and the SIMBA project (Davé et al. 2019).

Depending on the scientific goal of the study, different features of the cosmic web can be examined, often without relying on unequivocal definitions. Consequently, several algorithms have been developed to identify the cosmic web, some tailored for simulations and others for observational data, as illustrated in the exhaustive review by Libeskind et al. (2018). The different algorithms generally converge on the identification and characterization of specific features, but they reflect the complexity involved in the study and definitions of these structures.

In particular, the most used extraction methods can be grouped as graph and percolation techniques (e.g. MST, Alpaslan et al. (2014) and T-Rex, Bonnaire et al. (2020)), stochastic methods (e.g. Bisous model, Tempel et al. (2016)), methods based on the Hessian of the density, tidal or velocity fields (e.g. T-

web, Forero-Romero et al. (2009), V-web, Hoffman et al. (2012)) and, among these, those that follow a multi-scale approach (e.g. MMF, Aragón-Calvo et al. (2007), NEXUS and NEXUS+, Cautun et al. (2013). Moreover, the cosmic web can be identified with topological methods (e.g. Spinweb, Aragón-Calvo et al. (2010a) and DisPerSE, Sousbie (2011); Sousbie et al. (2011)) and, lastly, phase-space methods (e.g. ORIGAMI, Falck et al. (2012)).

In addition to the galaxy clusters, filaments constitute the densest regions of the cosmic web, containing approximately 50% of the matter in the Universe (Cautun et al. 2014). Filaments serve an important function in the accretion phase of galaxy clusters, acting as pathways for matter transportation towards the centre of the node to which they are connected. The connectivity of the cosmic web, which measures the number of filaments connected to a cluster, offers a method to quantify the interaction between clusters and the filaments surrounding them, enabling the assessment of structural evolution (Codis et al. 2018). Several works in literature have been investigating the correlation of connectivity and the cluster’s properties, such as the mass and the dynamical state (see e.g. Darragh Ford et al. 2019; Sarron et al. 2019; Malavasi et al. 2020b; Gouin et al. 2021; Galárraga-Espinosa et al. 2024).

Furthermore, several studies proved a significant role of filaments in the so-called ‘pre-processing’ of the galaxies that reside within the filamentary structures. Filaments affect galaxy evolution and galaxy properties, before entering the cluster, through several processes as ram-pressure, tidal effects and mergers (see the reviews of Boselli & Gavazzi (2006, 2014) and more recent works e.g. Kraljic et al. (2018); Winkel et al. (2021); Hellwing et al. (2021); Song et al. (2021); Donnan et al. (2022); Kotecha et al. (2022); Kuchner et al. (2022); Malavasi et al. (2022); Galárraga-Espinosa et al. (2024); Bulichi et al. (2024)). Therefore, the outskirts of clusters provide a distinctive environment for examining matter accretion dynamics and galaxy properties.

Unlike the galaxy content of filaments, which has been extensively identified with galaxy surveys, the detection of the gas component has proved to be more challenging. Hydrodynamical simulations (see e.g. Bond et al. 1996; Davé et al. 2001; Shull et al. 2012; Tuominen et al. 2021) predict that the filamentary structures of the cosmic web are hosting a large fraction of the *missing* baryons¹ in a low-density and warm-hot state known as Warm-Hot Intergalactic Medium (WHIM), with a density $\delta_b \approx 10 - 100$ and a temperature in the range of $10^5 - 10^7$ K.

The *hot* phase of WHIM, with a $\log T(K) \approx 5.5 - 7$, is not observable through absorption, being fully ionised, contrary to the low-temperature phase, with a $\log T(K) \approx 5 - 5.5$, which has been detected several times through metal absorption lines (Danforth et al. 2016). Despite having a faint emission, several attempts have been made to detect the warmest phase of WHIM through direct X-ray observations (see e.g. Eckert et al. 2015; Nicastro et al. 2018) and the Sunyaev-Zel’dovich effect, employing stacking methods (Tanimura et al. 2019, 2020, 2022) or looking at the densest regions between two close galaxy clusters (Bonjean et al. 2018; Hincks et al. 2022).

In this work, we use the outputs of THE THREE HUNDRED (Cui et al. 2018a) hydrodynamical simulations to extract the cosmic web in the surrounding volumes of galaxy clusters, with a spe-

¹ When compared to the concordance cosmology model, we observe a $\approx 30\%$ deficit in the census of observed baryons from low-redshift sources, such as galaxies, groups and clusters, inter-galactic and circum-galactic medium.

cific focus on the filamentary structures, from the gas particle distribution using the cosmic web finder DisPerSE. By analysing the connectivity estimates of simulated galaxy clusters, this investigation explores the influence of filaments on the main properties of galaxy clusters, such as their mass and dynamical state, and assess the cosmic web extraction from diffuse gas particles within the simulated THE THREE HUNDRED regions.

This paper is structured as follows: Sect. 2 provides a detailed overview of the THE THREE HUNDRED simulation and the theoretical framework behind the cosmic web finder DisPerSE. The process of creating the gas density maps and calibrating DisPerSE is discussed in Sect. 3. In Sect. 4 we present the results of the connectivity analysis, while in Sect. 5 we investigate the effect of cosmic web tracers by comparing the gas-traced filaments to mock-galaxy-traced filaments. Finally, Sect. 6 summarizes the main results of our study.

2. Simulation and methods

2.1. THE THREE HUNDRED project

The data set analysed in this work is extracted from THE THREE HUNDRED project² (Cui et al. 2018a). THE THREE HUNDRED hydrodynamical simulation consists in 324 zoom-in re-simulated regions centered on the most massive haloes selected at $z = 0$ from the MultiDark Planck 2 (hereafter as MDPL2) simulation (Klypin et al. 2016). MDPL2 is a DM-only cosmological simulation, consisting of a periodic cube with a side length of $1 h^{-1}$ Gpc with 3840^3 DM particles, each with a mass of $1.5 \times 10^9 h^{-1} M_\odot$. The cosmological parameters used in MDPL2 and THE THREE HUNDRED are those reported in the 2015 *Planck* data release (Planck Collaboration XIII 2016) ($h = 0.678$, $n_s = 0.96$, $\sigma_8 = 0.823$, $\Omega_\Lambda = 0.693$, $\Omega_M = 0.307$, and $\Omega_B = 0.048$).

The 324 spherical regions of THE THREE HUNDRED, centered on the most massive haloes ($M_{vir} > 8 \times 10^{14} h^{-1} M_\odot$), have a radius of $15 h^{-1}$ Mpc. The DM particles within these regions are split into separate dark matter and gas particles, according to the cosmological baryonic mass fraction, with masses $m_{DM} = 12.7 \times 10^8 h^{-1} M_\odot$ and $m_{gas} = 2.36 \times 10^8 h^{-1} M_\odot$.

In this analysis, we use the regions re-simulated with the smoothed particle hydrodynamics (SPH) code GADGET-X (Springel 2005; Beck et al. 2016) - a modified version of the GADGET3 code - which implements radiative cooling and star formation (Springel & Hernquist 2003), chemical stellar evolution (Tornatore et al. 2007), super massive black hole (BH) accretion and active galactic nuclei (AGN) and Supernovae feedbacks (Steinborn et al. 2015). The haloes and subhaloes within each region are identified with the publicly available³ Amiga Halo Finder (AHF; Knollmann & Knebe 2011), which includes DM, gas, stars and BHs in the density peak finding process and estimates the coordinates and properties of the clusters, such as their mass, radius and luminosities at various overdensities. The simulation runs are stored in 129 snapshots, from redshift $z = 17$ to $z = 0$.

In this work, we analyse the galaxy clusters’ catalogues at redshift $z = 0$, $z = 1.03$ and $z = 2.02$, which span, at $z = 0$, a mass range of $10^{13} \leq M_{200} h^{-1} M_\odot \leq 2.62 \times 10^{15}$.

² <https://the300-project.org>

³ <http://popia.ft.uam.es/AHF/>

2.2. DisPerSE

The cosmic web in the simulated regions is extracted using the publicly available⁴ Discrete Persistent Structure Extractor (DisPerSE; Sousbie 2011; Sousbie et al. 2011). DisPerSE is a topological structure finder, designed to identify multi-scale structures. It relies on the Discrete Morse theory (Forman 1998; Gyulassy et al. 2008) to identify the critical points of density fields. The noise introduced into the detection by the finite sampling of the density field is reduced with the approach of the Persistent homology theory (Edelsbrunner et al. 2002) and topological simplification (Edelsbrunner et al. 2002; Gyulassy et al. 2008).

In short, from a given 2D or 3D distribution of tracers, DisPerSE provides the position of the extreme points – where the gradient of the field is null – and the integral lines that connect them, which form the filaments. The starting point of DisPerSE can either be a catalogue of the tracers’ coordinates (e.g. galaxies or haloes) or a pixelated density map, as used in this work. In the first case, the density field is extracted from the Delaunay tessellation of the distribution with the Delaunay Tessellation Field Estimator (DTFE; Schaap & van de Weygaert 2000; van de Weygaert & Schaap 2009).

From the density field, the identified extreme points are classified as maxima, minima, saddle and bifurcation points, i.e. where a filament splits in two. The ridges are presented as a set of segments that connect two extreme points – usually a maximum and a saddle point – following the density field. The robustness of filaments, i.e. their reliability, is quantified through a threshold parameter called *persistence cut*, defined as the absolute difference of the density value of the two critical points at the filament’s extremes. The choice of the persistence allows for low-significance and noisy structures to be filtered out.

3. Cosmic web extraction

3.1. DisPerSE calibration

In order to extract a significant filamentary skeleton from the density distribution, a combination of parameters – the Gaussian smoothing of the input density map and the persistence cut of DisPerSE – needs to be tuned. The first step of the cosmic web extraction is the smoothed gas density field reconstructed from the regions of the hydrodynamical simulation. THE THREE HUNDRED gas-traced cosmic web has been widely analysed in previous works, namely to study the properties of filaments (Rost et al. 2021, 2024) and as a benchmark for the identification of galaxy-traced filaments (Kuchner et al. 2020, 2021). In this work, we choose to analyse the filamentary structures traced from the gas particle distribution because we plan, in future studies, to use 3D gas filaments and their projection as a benchmark for the detection of filaments from mock Compton- γ maps generated in THE THREE HUNDRED simulation, as described in Cui et al. (2018a).

The gas particles of each simulated region were first binned in a 3D grid of $30 h^{-1}$ Mpc per side, with a pixel resolution of $150 h^{-1}$ kpc. Then, to avoid sharp variations from one pixel to another, we applied a Gaussian kernel to smooth the density field. As the smoothing kernel of the map increases, only the more distinct structures will be identified by the filament finder, leading to a network that only features robust critical points and filaments. For this analysis, we applied a Gaussian kernel with a full width at half-maximum (FWHM) of 4 pixels, equivalent to $600 h^{-1}$ kpc. We opted for this specific kernel size, ensuring it

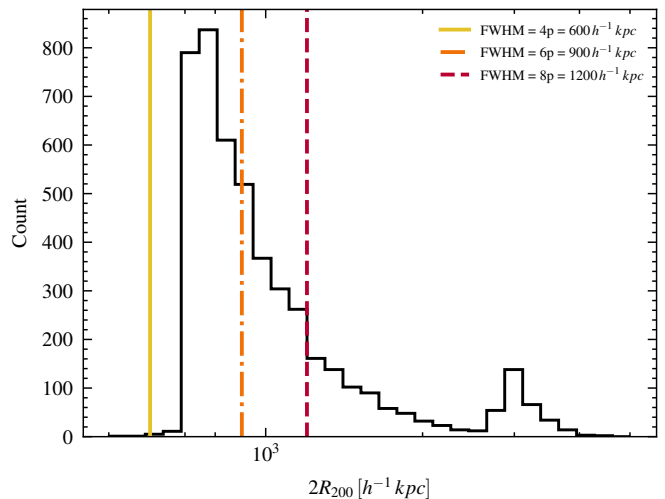


Fig. 1: Diameter $2R_{200}$ distribution of galaxy clusters at $z = 0$. The vertical lines represent the smoothing kernel FWHM at 4, 6, and 8 pixels, respectively in yellow (solid), orange (dot-dashed) and red (dashed).

remains smaller than the diameter of the galaxy clusters that we analysed, to preserve the resolution of these structures, as shown in Fig. 1, where we compare the chosen value and two larger smoothing kernels to the distribution of the diameters of clusters at $z = 0$.

In addition to the smoothing level of the density map, the robustness of the extracted network depends also on the DisPerSE parameter *persistence*. The effect of the persistence cut on the network is similar to the Gaussian smoothing, with higher values of persistence leading to less critical point pairs and therefore to the removal of less significant filaments. The optimal value of persistence cut for our data set is 0.5, which identifies the threshold between significant topological features and noisy ones as seen in the DisPerSE Persistence Diagram Viewer (pdview), accessible with the option `-interactive` of the function `mse`. The density maps are first analysed by DisPerSE with the function `mse`, with the options `-forceLoops`, `-periodicity 000`, `-cut 0.5` and `-upSk1`, to compute the Morse-smale complexes. During this step, the filaments are extracted and the critical points are identified. Then, the networks are post-treated with the function `skelconv`, which we implemented with the following options: `-smooth 1`, `-breakdown`, `-rmOutside` and `-rmBoundary`. Here, the option `-breakdown` merges the infinitely close pieces of arcs and adds the bifurcations points, while the `-smooth` option determines the straightness of the filament’s trace, while keeping the critical points coordinates fixed. We note that the `-smooth` function does not affect the extraction and positions of filamentary structures and, although having a similar name, is different from the Gaussian smoothing kernel applied on the density maps, which operates on the density field prior to the cosmic web extraction procedure on DisPerSE.

3.2. Simulated cosmic web network

In the DisPerSE output networks, the galaxy groups and clusters are defined only by the coordinates of the maxima (the nodes), while the filaments are defined only by the position of their spines. To associate the extracted skeleton to the density distribution of the simulation, one needs to match the nodes to

⁴ <https://www2.iap.fr/users/sousbie/web/html/indexd41d.html>

THE THREE HUNDRED galaxy clusters, identified with AHF. While there are several ways to associate the nodes to clusters (for a complete study we refer the reader to Cohn 2022), in this analysis we require the distance between the coordinates of the node and the cluster to be less than the smoothing kernel of 4 pixels. Where multiple pairs that satisfy this condition, we match the DisPerSE node to the nearest AHF cluster.

To evaluate the accuracy of the DisPerSE catalogue and of the matches, we can compute the completeness of the sample, defined as the number of groups and clusters matched to nodes, normalized by the total number of groups, as in Cornwell et al. (2024). The completeness depends on the smoothing scale of the density maps, with a larger and less filtering smoothing kernel resulting in lower completeness of the sample, as shown in Fig. 2. Here, we display the completeness of the sample as a function of the Gaussian smoothing FWHM, averaged over the 324 simulated regions. To test only the effect of the smoothing scale on the completeness of the sample, we use the same persistence cut for all the smoothing values, which alters the skeleton in a similar way of the smoothing. This result agrees with Cohn (2022) and Galárraga-Espinosa et al. (2024), where they studied the effect of the smoothing on the completeness respectively on skeletons extracted from dark matter and galaxies distributions.

The sample analysed in this work has an average completeness value of 89%, indicating that almost every group or cluster identified in the simulated regions has a matched DisPerSE node. It is worth noticing that since the completeness is lower than the ideal value of 100%, some clusters remain unmatched by any DisPerSE nodes. This discrepancy might be attributed to their coordinates' distance exceeding the threshold we set. This phenomenon could be explained by considering that DisPerSE node coordinates are determined solely from the gas-only density distribution, unlike cluster coordinates, which also incorporate data from dark matter particles. Therefore, the different spatial distributions of dark matter and gas particles near the centre of the regions could affect the peak density finding process (Cui et al. 2018b; Lokken et al. 2023). Conversely, there are DisPerSE nodes without any corresponding clusters. This population of nodes likely represents local maximum points of the density field not classified as haloes by AHF or nodes associated to sub-haloes. To avoid possible contamination by low-resolution DM particles near the borders, we consider only the matched nodes inside a sphere of $13 h^{-1}$ Mpc radius from the centre of each region. Lastly, we note that the galaxy groups and clusters analysed in this work - except the 324 most massive ones - reside within the $15 h^{-1}$ Mpc environment of very massive galaxy clusters ($M_{vir} > 8 \times 10^{14} h^{-1} M_{\odot}$).

The final sample used for this analysis, including all the 324 simulated regions, amounts to 3412 galaxy groups and clusters and 12 643 filaments at $z = 0$. The filament sample includes filaments going from a maximum point to another - with a saddle point in the middle -, filaments from one maximum point to a bifurcation point and filaments with two bifurcation points at the extremes. The filament length distribution, computed as the sum of the lengths of all segments belonging to each filament, is shown in Fig. 3, along with the median values of the distribution. We plot the length distribution of the whole sample in black, in red the length distribution of maximum-maximum filaments and in grey the length of bifurcation-maximum and bifurcation-bifurcation filaments. The mean length of the maximum-maximum filaments is $6.67 h^{-1}$ Mpc, comparable to the length of filaments extracted in Rost et al. (2021) from the same gas particle distribution but with different levels of smoothing of the density map and persis-

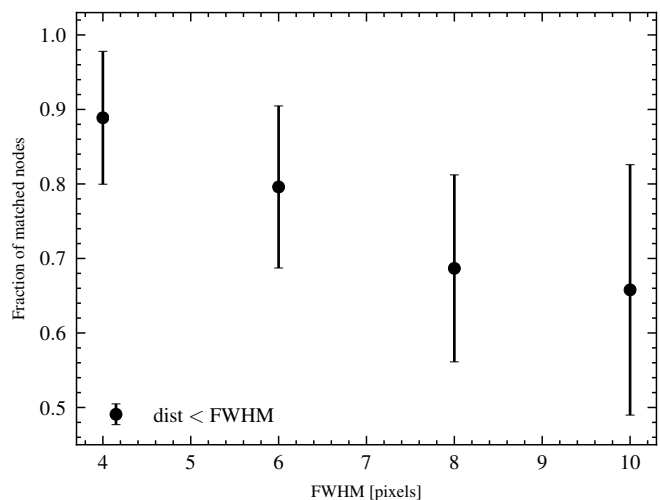


Fig. 2: Completeness of the sample. Each dot refers to the completeness of the sample, averaged over the 324 simulated regions, extracted with different smoothing kernels. The error bars represent the standard deviation error.

tence. Due to the exploration of the limited volume of each region, compared to different studies in literature, the extracted filaments predominantly belong to the short filaments population, as shown in previous studies (Bond et al. 2010a; Galárraga-Espinosa et al. 2020).

An example of a simulated region at $z = 0$ is shown in Fig. 4a. Here, we display the whole simulated skeleton in grey, while the critical points are represented in the following way: the nodes as red stars, the saddle points as blue dots and the bifurcation points as yellow triangles. Moreover, we plot the R_{200} spheres of the matched central cluster and less massive groups in the region. A zoom-in of the central cluster and an example of bifurcation points inside the R_{200} sphere are displayed in the bottom panels of the figure, respectively in Figs. 4b and 4c.

4. Results

To investigate the dependence of cosmic web filaments on the properties of galaxy clusters, we estimate the connectivity of clusters, denoted with k . The connectivity of a galaxy cluster, as defined by Codis et al. (2018), is the number of filaments globally connected with the cluster. More specifically, the connectivity is the number of filaments connected to the galaxy cluster at a specific aperture, or in other words, the number of filaments intersecting the surface of a sphere with a certain radius R_{Δ} ⁵.

For the complete data set, we estimate the connectivity of groups and clusters at R_{500} , R_{200} and R_{vir} , denoted respectively as k_{500} , k_{200} and k_{vir} , where the subscript *vir* refers to the virial radius⁶. With this definition, the connectivity value takes into account filaments that start from a node or a bifurcation point within the aperture considered. An example of this phenomenon is displayed in the bottom right panel of Fig 4c, where the cluster has a connectivity k_{200} equal to 7, considering the filaments originating from the bifurcation points inside R_{200} . We observe

⁵ The subscript Δ represents the overdensity, i.e. value of the ratio between the density of the cluster inside that radius and the critical density of the Universe $\rho_c = 3H^2/(8\pi G)$ at the cluster's redshift.

⁶ The virial radius refers to the aperture where the halo satisfies the conditions of the virial theorem.

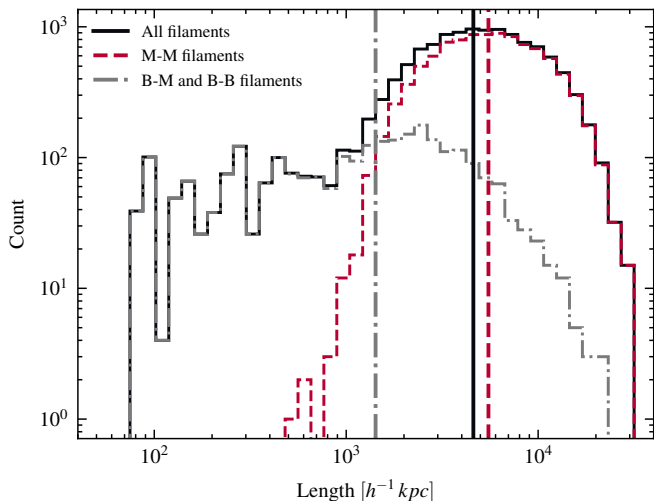


Fig. 3: Filaments length distribution. In the black solid line we plot the distribution of length for the whole sample of filaments. In the red dashed line, the length distribution of the filaments with two maxima at the extremes and in the grey dot-dashed line the length of bifurcation-maximum and bifurcation-bifurcation filaments. The vertical lines are the median values of each distribution.

that, for the sake of redundancy, we omit from the connectivity symbol the subscripts denoting the cosmic web tracer and dimensionality, which in our case should be gas and $3D$, although these aspects should always be specified when considering the cosmic web identification.

4.1. Connectivity and galaxy cluster mass

The number of filaments connected to a galaxy cluster – the connectivity – is expected to scale with the cluster’s mass. As filaments feed the cluster centre with dark matter, gas and galaxies, more connected clusters are on average more massive.

In THE THREE HUNDRED data set, we estimate the connectivity for 3412 groups and clusters at $z = 0$, with a total mass range of $10^{13} \leq M_{200} h^{-1} M_{\odot} \leq 2.62 \times 10^{15}$. Our results of the connectivity as a function of the cluster’s mass M_{200} at $z = 0$ are presented in Fig. 5. We find the expected correlation between the mass and k at all the apertures explored – R_{500} , R_{200} and R_{vir} – whose mean values and errors on the mean, computed with the bootstrap method⁷, are plotted respectively in red, pink and blue. We performed linear fittings, plotted as dashed lines in Fig. 5 and whose parameters are shown in Table 1, as the following: $\log k_{\Delta} = A \cdot \log M_{200} + B$.

Table 1: The fitting parameters for the $\log k_{\Delta} - \log M_{200}$ relation

Aperture	A	B
R_{500}	0.295 ± 0.016	-3.69 ± 0.24
R_{200}	0.308 ± 0.019	-3.86 ± 0.27
R_{vir}	0.324 ± 0.021	-4.09 ± 0.30

⁷ For the bootstrap re-sampling, we draw 1000 new samples with replacement, i.e. the same data point can be selected several times, each sample with the same length as the original sample. The error is the standard deviation of the new distribution.

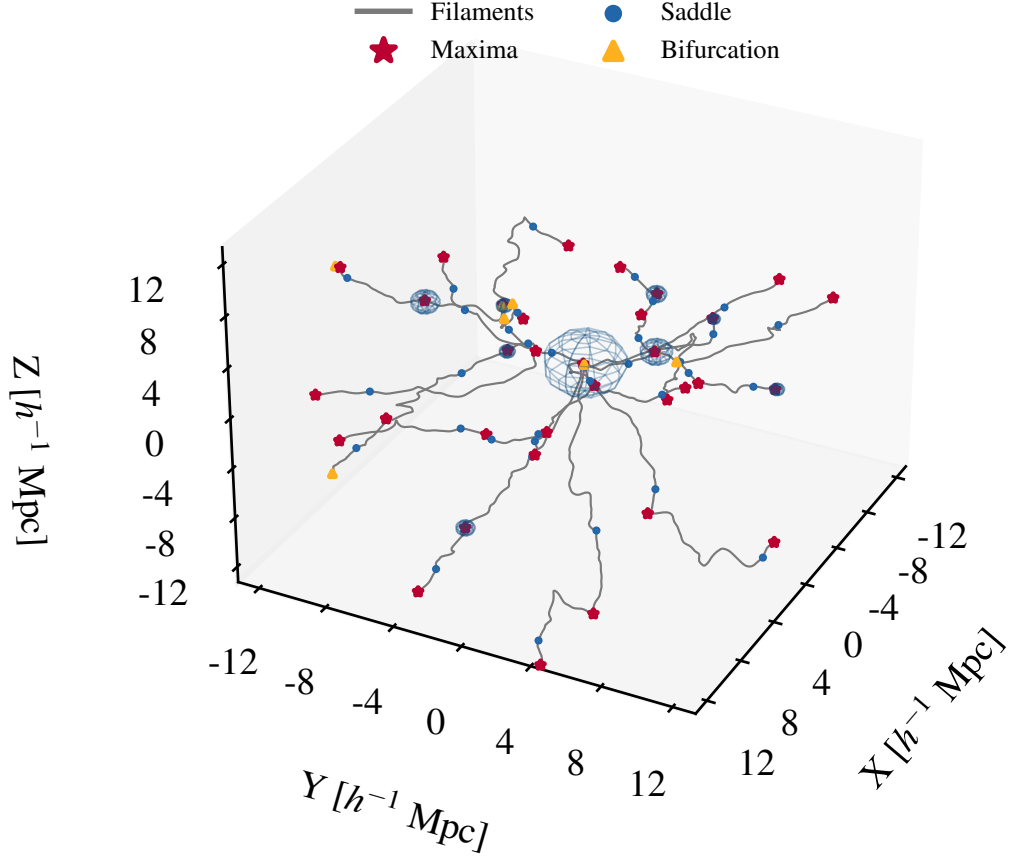
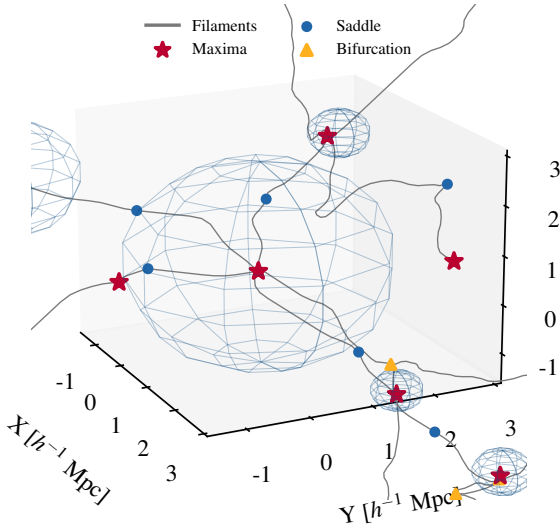
We observe a flattening in the growing trend among low-massive clusters, specifically in the range $13 \leq \log[M_{200}/h^{-1} M_{\odot}] \leq 14.5$, not present for the massive and central clusters. This phenomenon is likely attributed to the intrinsic limitation on the minimum connectivity value, introduced by our sample construction, which can not be less than one. The clusters for which we compute the connectivity are, in fact, matched to DisPerSE critical nodes, which are, by definition, all linked to at least one filament.

A direct computational consequence of including other critical points, besides the node matched to the cluster, inside the aperture in the estimate of the connectivity is that the connectivity depends on the aperture chosen, with k_{vir} always equal to or larger than k_{200} and k_{500} . This result is also visible in Fig. 5. We note that this effect is more evident for more massive clusters – the clusters at the centre of the simulated boxes – which lie in a denser environment and can have several substructures, leading to more nodes identified by DisPerSE. Further studies are needed to investigate other physical explanations of this phenomenon, such as the diffusion of filaments inside the apertures considered. This result is consistent at larger redshifts, namely for $z = 1$ and $z = 2$, as shown in Appendix A.

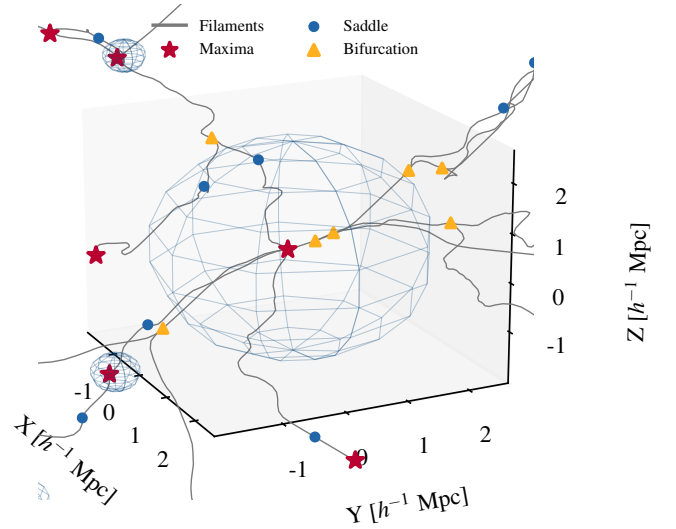
Finally, it’s worth noting that the linear fits and the findings shown in Fig. 5 are computed based on a constant mass, M_{200} , for both the dataset at R_{500} and R_{vir} . This decision was made specifically to emphasize how the connectivity of a fixed cluster mass varies with the aperture. Nevertheless, it’s important to mention that the positive correlation between the connectivity and mass would persist even if we were to consider the general relationship between $k_{\Delta} - M_{\Delta}$.

Our measurements of the connectivity show a strong agreement with other connectivity values from literature, over a wider mass range. This result is shown in Fig. 6, where we plot THE THREE HUNDRED data compared to other connectivity samples from literature, estimated from simulations and observations. The data of Aragón-Calvo et al. (2010b), plotted as blue triangles, are derived from a Λ cold dark matter N-body simulation, where a multiscale morphological filter (MMF; Aragón-Calvo et al. (2007)) was used to extract cosmological structures as walls, clusters and filaments. The values of Gouin et al. (2021) and Galárraga-Espinosa et al. (2024) are estimated from hydrodynamical simulations, respectively, the IllustrisTNG and the MilleniumTNG and are plotted as grey dots (relaxed groups) and crosses (unrelaxed groups) and as pink triangles. The connectivity value of the simulated Coma cluster of Malavasi et al. (2023), plotted as violet diamond, is estimated from a dark matter-only N-body simulation. The observed samples are the AM-ASCFI clusters sample, plotted as green stars, extracted from the CFHTLS photometric redshift survey of Sarron et al. (2019) and the COSMOS2015 photometric redshift catalogue of Dargh Ford et al. (2019), plotted as yellow squares. Lastly, the observed connectivity value of the Coma cluster in Malavasi et al. (2020b) is computed from the cosmic web extracted from the Main Galaxy Sample of the Sloan Digital Sky Survey (SDSS) (Malavasi et al. 2020a) and plotted as a red diamond.

Although the connectivity values span almost the same ranges, it is important to note the differences in how measurements were taken. This difference may include variations in how the connectivity is defined and at which aperture is estimated, the type of tracers used to extract the cosmic web and the filament finder employed. In particular, the connectivity can be computed at a fixed aperture for all the clusters, as in Aragón-Calvo et al. (2010b), where they adopt a fixed aperture of $3 h^{-1}$ Mpc, and in Sarron et al. (2019), with a fixed aperture of 1.5 cMpc, or it can


(a) Filaments in region 1 at $z = 0$


(b) Zoom-in of a central cluster



(c) Example of bifurcation points inside the cluster

Fig. 4: Examples of DisPerSE simulated networks. The top panel (a) shows the full filament network of region 1 in grey. The nodes are shown as red stars, the saddle points as blue dots and the bifurcation points as yellow triangles. The light blue spheres are the R_{200} of matched clusters. The bottom left panel (b) is a zoom-in of the central cluster of region 6. The bottom right panel (c) is an example of two bifurcation points inside the R_{200} sphere of the central cluster of region 2.

be estimated at a set overdensity, as in the case of [Darragh Ford et al. \(2019\)](#) and [Malavasi et al. \(2020b, 2023\)](#), whose connectiv-

ity is at $1.5 R_{vir}$ or as [Gouin et al. \(2021\)](#) and [Galárraga-Espinosa et al. \(2024\)](#), with an aperture of $1.5 R_{200}$.

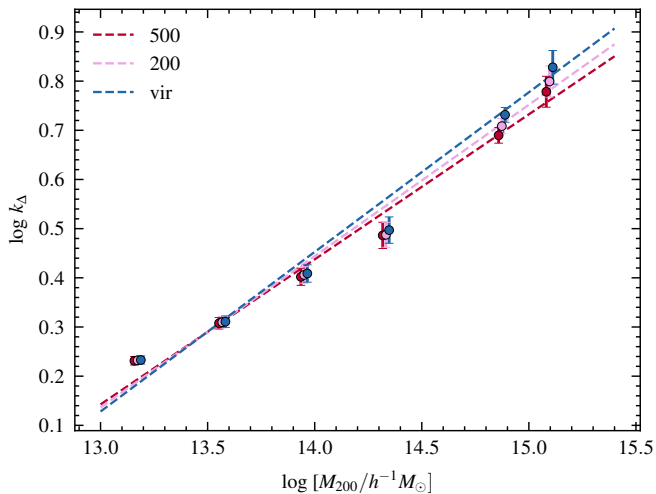


Fig. 5: The mean connectivity of THE THREE HUNDRED groups and clusters at $z = 0$ as a function of the mass M_{200} . The connectivity is estimated at different over-densities, respectively k_{500} in red, k_{200} in pink and k_{vir} in blue. The dashed lines represent the linear fitting. The error bars are the errors on the mean values, computed with the bootstrap method, multiplied by 2 for visual clarity. The mean values are shifted in mass for visual clarity.

The different web finder employed can also affect the recovery of the filamentary structures – and therefore the estimate of the connectivity – since they rely upon different approaches (we refer the reader to Libeskind et al. (2018) for a review of the most common web finders). The most used filament finder is DisPerSE, employed in this work as well as in Sarron et al. (2019); Darragh Ford et al. (2019); Malavasi et al. (2020b, 2023) and Galárraga-Espinosa et al. (2024), although with different parameters tuning. The cosmic web in Gouin et al. (2021) is extracted with the graph-based algorithm T-ReX (Bonnaire et al. 2020).

The final distinction to consider is the type of tracers used to extract the web. In this work, the filamentary structures are traced by the gas particle distribution, in Aragón-Calvo et al. (2007) by dark matter particles, while the remaining studies make use of observed or simulated galaxy catalogues.

All the previous studies confirm a positive correlation between the number of filaments connected to a cluster and its mass, thus affirming the significant role filaments play in the accretion of matter towards the clusters. However, it is important to take the possible biases into account, summarized in Table 2, when referring to the connectivity.

4.2. Connectivity evolution with redshift

According to the standard theory of anisotropic collapse (Zel'dovich 1970), matter in the universe is predicted to flow from less dense to denser regions over cosmic time, progressing from walls to filaments and eventually to clusters. As a consequence, in recent times the universe is predominantly composed of large under-dense regions – the voids – in terms of volume, while clusters and filaments dominate in terms of mass. Moreover, it has been shown (see e.g. Cautun et al. (2014)) that, at high redshift, the filaments of the cosmic web are dominated by thin structures, which are then prevailed by more significant ones at later times. In this framework, we investigate the evolution of cluster connectivity with redshift, which is expected to decrease

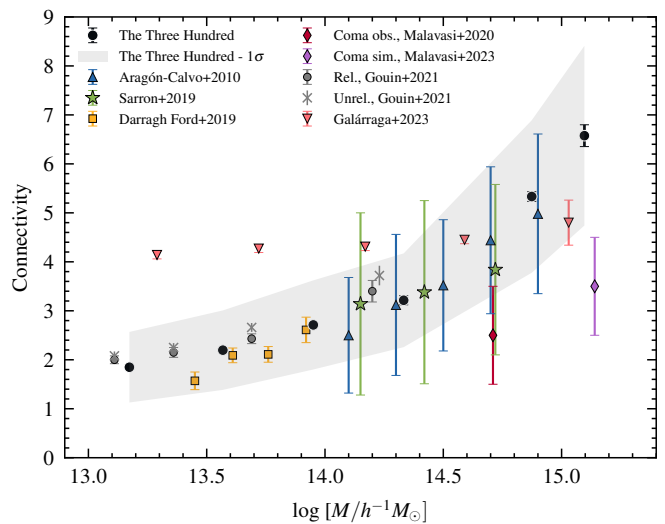


Fig. 6: Connectivity of THE THREE HUNDRED clusters compared to literature values (see the legend for details). The black dots are the mean connectivity values k_{200} of THE THREE HUNDRED groups and clusters. The error bars of THE THREE HUNDRED points are the errors on the mean, estimated with the bootstrap method, while the shaded grey area is the standard deviation error. For the literature values, the error bars represent the error on the mean, except for the data set of Aragón-Calvo et al. (2010b); Sarron et al. (2019); Malavasi et al. (2020b) and Malavasi et al. (2023). For details and differences of each sample see the main text and Table 2.

with cosmic time, as shown in Codis et al. (2018) and Galárraga-Espinosa et al. (2024).

To detect the cosmic web skeletons at higher redshifts, we create the density maps from the gas particle distributions at redshift $z = 1.03$ and $z = 2.02$, with the same parameters used for the $z = 0$ sample, with a pixel resolution of $150 h^{-1}$ kpc and a Gaussian smoothing with a FWHM of 4 pixels. We use the same DisPerSE functions and persistence cut of 0.5, in order to extract filamentary structures with the same robustness and significance. The two final samples have a completeness value of 82% and 83%, respectively at redshift $z = 1$ and $z = 2$, indicating that almost every cluster is matched by a node, similar to the sample at $z = 0$.

We compare the connectivity mean values estimated at R_{200} of clusters in the mass range of $10^{13} \leq M_{200} h^{-1} M_{\odot} \leq 10^{14}$, populated at all the redshifts explored. In Fig. 7 we plot the connectivity values at $z = 0$ in red, $z = 1$ in purple and $z = 2$ in yellow. We recover the expected trend of the connectivity decrease from high redshift to present times, in agreement with what has been found both in theoretical predictions from 2D and 3D estimates (Codis et al. 2018) and, more recently, in hydrodynamical simulations (Galárraga-Espinosa et al. 2024). We observe that, for masses below $2.5 \times 10^{13} h^{-1} M_{\odot}$, the connectivity at $z = 0$ shows a flattening trend and remains comparable to the values of higher redshifts. A possible reason for this behaviour can be found in the intrinsic minimum connectivity value introduced by the sample construction, as explained in detail in Subsect. 4.1.

The decrease of connectivity with cosmic time is both a consequence of the anisotropic collapse of the cosmic web structures, with two filaments that merge into one, or a result of their stretch and disconnection caused by the cosmological expansion of voids regions in later times due to the dark energy. However,

Table 2: A summary of the parameters of previous literature studies compared to this work.

Sample	Data	k_R	Mass	CW extraction	Web finder	References
The300	Hydro-sim	R_{200}	M_{200}	3D gas particles	DisPerSE	this work
N-body sim	DM-sim	$3 h^{-1}$ Mpc	M_{vir}	3D DM particles	MMF	1
AMASCFI	Observations	$1.5 h^{-1}$ Mpc	M_{200}	2D galaxies	DisPerSE	2
COSMOS2015	Observations	$1.5 R_{vir}$	M_{200}	2D galaxies	DisPerSE	3
Coma obs.	Observations	$1.5 R_{vir}$	M_{200}	2D galaxies	DisPerSE	4,5
Coma sim.	DM-sim	$1.5 R_{vir}$	M_{200}	2D galaxies	DisPerSE	6
IllustrisTNG	Hydro-sim	$1.5 R_{200}$	M_{200}	3D galaxies	T-ReX	7
MilleniumTNG	Hydro-sim	$1.5 R_{200}$	M_{200}	3D galaxies	DisPerSE	8

References. (1) Aragón-Calvo et al. (2010b); (2) Sarron et al. (2019); (3) Darragh Ford et al. (2019); (4) Malavasi et al. (2020b) (5) Malavasi et al. (2020a); (6) Malavasi et al. (2023); (7) Gouin et al. (2021); (8) Galárraga-Espinosa et al. (2024).

further research is required to explore the influence of matter inflow from walls to filaments on filamentary evolution with cosmic time. We note that future studies of the evolution of connectivity with redshift with different dark energy models (see e.g. Codis et al. 2018), and critical events, such as filaments mergers (see e.g. Cadiou et al. 2020), could offer an interesting probe for dark energy models.

cluster mass M_Δ :

$$f_s = \frac{\sum_i M_i}{M_\Delta} \quad (1)$$

The center-of-mass offset Δ_r is defined as:

$$\Delta_r = \frac{|\mathbf{r}_{cm} - \mathbf{r}_c|}{R_\Delta} \quad (2)$$

where \mathbf{r}_{cm} is the position of the centre-of-mass and \mathbf{r}_c is the theoretical centre of the cluster, defined as the highest density peak, which typically coincides with the brightest cluster galaxy (BCG). The Δ_r parameter is used to describe the cluster's deviation from smoothness and spherical symmetry, as objects with high values of Δ_r are considered morphologically disturbed.

Specifically, we classify the clusters as *relaxed* if both the conditions $f_s < 0.1$ and $\Delta_r < 0.1$ are simultaneously satisfied. On the other hand, a cluster is classified as dynamically *disturbed* if both $f_s > 0.1$ and $\Delta_r > 0.1$ are true. The clusters whose indicators are not simultaneously verified – therefore if $f_s > 0.1$ and $\Delta_r < 0.1$ or if $f_s < 0.1$ and $\Delta_r > 0.1$ – are classified as *hybrid*.

We estimate the dynamical state of the clusters at redshift $z = 0$ and compute the degree of relaxation as in Eq. 3, considering the parameters at R_{200} . In our sample, 66% of the clusters are classified as relaxed, 20% as hybrid and 14% as disturbed. In Fig. 8, we plot the connectivity-mass relation, computed at R_{200} , for the three sub-samples of dynamical state, respectively relaxed clusters in green, hybrid in yellow and unrelaxed clusters in light blue. The three sub-samples overlap and are comparable to each other, within the errors estimated with the bootstrap method, indicating that the connectivity-mass relation is not affected by the dynamical state – assessed in terms of the two indicators f_s and Δ_r – of the cluster. This result is not dependent on the redshift, as shown in Appendix B, where we present this analysis at redshifts $z = 1$ and 2, nor on the overdensity at which the connectivity and the dynamical state are estimated, as shown in Appendix C, where we present the same analysis for R_{500} and R_{vir} .

To further investigate the relation between the dynamical state of the cluster and the filaments connected to it, we now focus on the continuous dynamical state indicator χ . The degree of relaxation combines the dynamical parameters in a single measure of the cluster dynamical state and is defined by Hagggar et al. (2020) as:

$$\chi = \left[\frac{\sum_i \left(\frac{x_i}{x_{0,i}} \right)^2}{N} \right]^{-1/2} \quad (3)$$

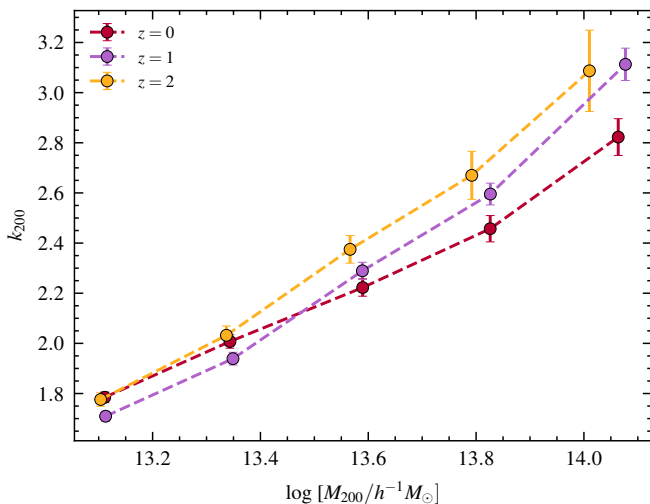


Fig. 7: Evolution with redshift of the connectivity-mass relation. In yellow, the mean values of connectivity k_{200} extracted from the gas skeleton at $z = 2$, in purple the values at $z = 1$, in red the values at $z = 0$. The error bars represent the errors on the mean, computed with the bootstrap method.

4.3. Connectivity and galaxy cluster dynamical state

To investigate if the filaments are related to the dynamical state of galaxy clusters or if the connectivity can be used as a tracer of the dynamical state, we study the correlation between the connectivity and the dynamical state of each cluster. In this work, we assess the dynamical state of a cluster following the definition of De Luca et al. (2021), based on 3D dynamical parameters estimated from the physical properties of each particle in the simulation. To evaluate the dynamical state in regions different from the virial radius volumes we consider two indicators of the cluster's dynamical state, the total sub-halo mass fraction f_s and the center-of-mass offset Δ_r . The total sub-halo mass fraction f_s is defined as the sum of all the sub-halo masses M_i , identified by AHF within a specific aperture R_Δ , normalized by the total

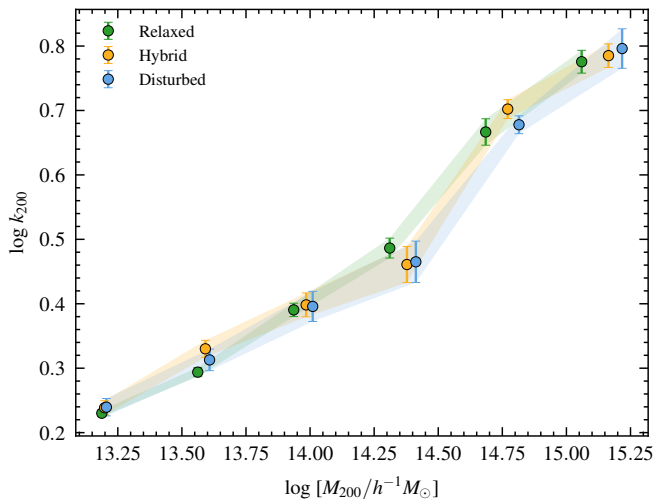


Fig. 8: Connectivity and mass relation for three dynamical state sub-samples at redshift $z = 0$. In green the connectivity mean values k_{200} for the dynamically relaxed clusters, in yellow for hybrid clusters, and in light blue the values for dynamically disturbed clusters. The error bars represent the errors of the mean, computed with the bootstrap method.

where x_i is the general indicator of the dynamical state, $x_{0,i}$ is the threshold between the relaxed and the disturbed regimes and N is the number of indicators used. As a result, larger values of χ (with $\log \chi > 0$) indicate a more relaxed dynamical state, while negative values of $\log \chi$ represent a disturbed dynamical state. In literature, the definition of the degree of relaxation can vary both in the choice of the parameters used and in the selection of the threshold values (see e.g. Cui et al. 2017). In this work, we estimate χ with f_s and Δ_r , both considered with a threshold of 0.1.

To possibly disentangle the impact of connectivity and mass on the dynamical state, given their correlation, we divide the total data set in three bins of connectivity and three bins of mass. This approach is necessary to study the relationship between the degree of relaxation and the connectivity independently of the mass, and vice versa.

The three connectivity bins divide the data set into ~ 700 weakly connected groups, with a $k_{200} < 2$, ~ 2000 average-connected clusters, with $k_{200} \in \{2, 3\}$, and ~ 500 highly connected clusters with $k_{200} > 3$. These thresholds were chosen taking the mean connectivity value of $k_{200} = 2.42$ of the whole cluster population at redshift $z = 0$ into account.

In the left panel (a) of Fig. 9 we plot the mean degree of relaxation as a function of the mass for the three connectivity sub-samples, respectively in green the weakly-connected, in yellow the average-connected and in light blue the highly connected clusters. At fixed mass, the three connectivity bins overlap and are comparable to each other within the errors, confirming that the connectivity does not influence the dynamical state of the cluster, computed with the f_s and Δ_r , corroborating the result shown in Fig. 8.

This outcome is not consistent with that of Guin et al. (2021) who found a correlation between the degree of relaxation and the connectivity values, with more connected clusters being on average more dynamically unrelaxed. We note that the disagreement could be due to the different definition of the degree of relaxation used in Guin et al. (2021), which differs from ours in the dynamical indicators and thresholds used, as well as the

differences in the data set and the cosmic web extraction as illustrated in Table 2.

Focusing now on the mass bins, we divide the data set into low-mass groups, with $M_{200} < 5 \times 10^{13} h^{-1} M_\odot$, medium groups and clusters, with $10^{13} \leq M_{200} h^{-1} M_\odot < 5.5 \times 10^{14}$ and massive clusters with $M_{200} \geq 5.5 \times 10^{14} h^{-1} M_\odot$, which correspond to the large galaxy clusters at the centre of each simulated region. The three sub-samples are plotted in the right panel (b) of Fig. 9, respectively in green, yellow and light blue. Contrary to the connectivity sub-samples shown in Fig. 9a, at fixed connectivity the three mass bins show a distinct separation from one another. This behaviour suggests a correlation between the degree of relaxation χ_{200} and the mass of the cluster, independently of their connectivity value, with less massive groups appearing to be more dynamically relaxed, and vice versa.

This result was also reported by Kuchner et al. (2020) – although with a different definition of the degree of relaxation, both in the parameters and the thresholds chosen – who suggest that the most massive clusters tend to be in a more dynamically disturbed state. This phenomenon is likely attributed to the fact that the most massive clusters are currently still in a growing-process, resulting in larger centre-of-mass offsets and in the presence of internal substructures (Power et al. 2012). Moreover, the high-density environment in which they are situated can make them more likely to accrete matter, resulting in less relaxed states (Kuchner et al. 2020).

4.4. Connectivity and mass bias

Classical approaches to infer the mass of galaxy clusters from SZ and X-rays observations usually rely on the hydrostatic equilibrium (HE) assumption (for a review, see Kravtsov & Borgani 2012). This hypothesis assumes that the gas thermal pressure is balanced by the gravitational forces, leading the cluster in a state of equilibrium. Deviations from the HE can introduce errors on the estimation of observable properties of clusters and their mass.

We investigate if the presence of filaments, quantified with the connectivity, has an impact on the hydrostatic equilibrium of the galaxy clusters of THE THREE HUNDRED simulation. For this purpose, we refer to the analysis of Gianfagna et al. (2023), who explored the deviations of the HE mass M_{HE} from the total mass M_{true} of the 324 simulated central clusters, quantified with the hydrostatic mass bias b . The M_{true} refers to the real mass, computed by summing all the DM, gas and stars particle masses inside a radius. On the other hand, the hydrostatic equilibrium mass M_{HE} is the mass inferred from the gas thermal pressure profile estimated from SZ observations or from the temperature and electron density profiles from X-rays observations, leading respectively to the mass biases b_{SZ} and b_X , defined as:

$$b = \frac{M_{true} - M_{HE}}{M_{true}} \quad (4)$$

We refer to Gianfagna et al. (2023) for the complete derivation of the parameters. We note that a positive bias, if defined in this way, denote an underestimation of the true mass.

We plot in Fig. 10 the median values of the hydrostatic mass biases b_{SZ} and b_X , estimated at R_{200} as a function of the connectivity k_{200} of the cluster. No correlation is found between the bias and the connectivity, independently of observable property used to estimate it. Moreover, we note that we do not observe any variation of the scatter with connectivity, meaning that the dispersion of the bias is independent of the number of filaments connected.

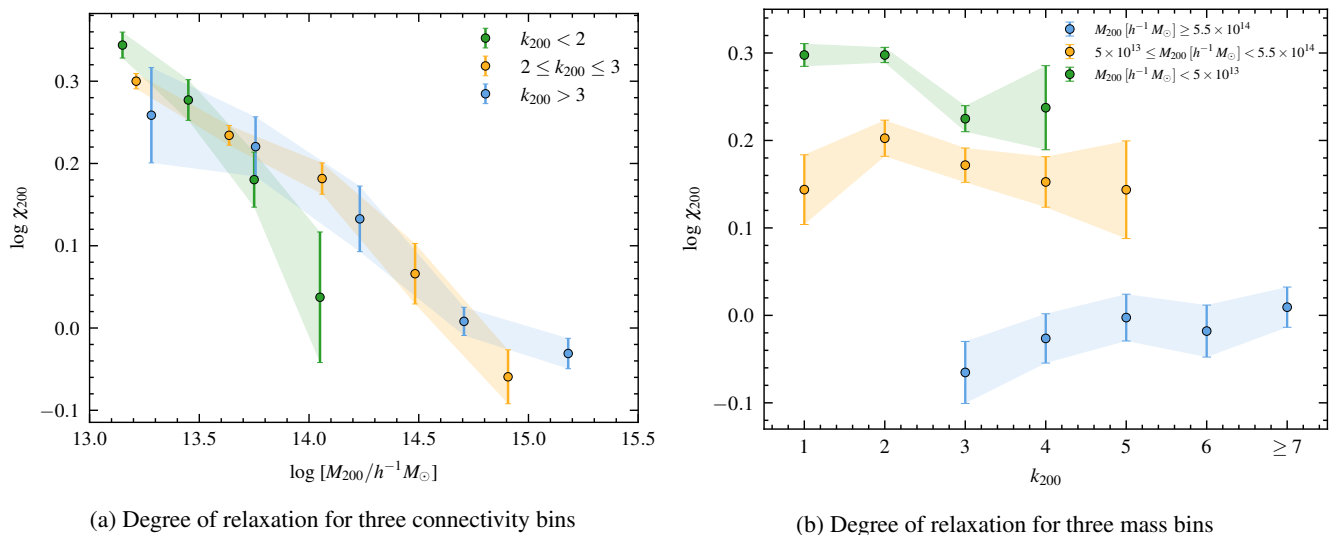


Fig. 9: Dynamical state dependence on connectivity and cluster total mass at redshift $z = 0$. The left panel (a) shows the degree of relaxation χ_{200} as a function of the total mass M_{200} . Green, yellow and light blue dots indicate respectively weakly connected ($k_{200} < 2$), average-connected ($k_{200} \in \{2, 3\}$) and highly connected ($k_{200} > 3$) clusters. The right panel (b) shows the degree of relaxation χ_{200} as a function of the connectivity k_{200} . Green, yellow and light blue dots indicate respectively low mass ($M_{200} < 5 \times 10^{13} h^{-1} M_{\odot}$), medium ($5 \times 10^{13} \leq M_{200} h^{-1} M_{\odot} < 5.5 \times 10^{14}$) and massive ($M_{200} \geq 5.5 \times 10^{14} h^{-1} M_{\odot}$) clusters. The shaded areas and the error bars indicate the error of the mean, computed with the bootstrap method.

On the other hand, the scatter of the hydrostatic mass bias has been found to vary as a function of the dynamical state, quantified with different indicators, with disturbed clusters showing a wider dispersion (Piffaretti & Valdarnini 2008; Rasia et al. 2012; Ansarifard et al. 2020; Gianfagna et al. 2023). This result suggests that the connectivity may not be used as a reliable indicator of the dynamical state of a galaxy cluster, as already shown in Sec. 4.3. The same result is observed for the connectivity and the bias estimated at R_{500} , as shown in Appendix D.

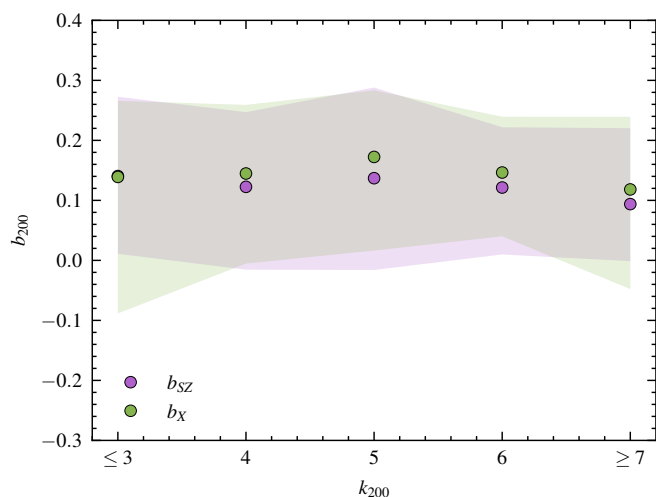


Fig. 10: Connectivity and hydrostatic mass bias relation at redshift $z = 0$. In green the mass bias median values b_X at R_{200} and in violet mass bias median values b_{SZ} at R_{200} . The shaded areas represent the 16th and 84th percentiles.

5. Mock-galaxy filaments

In this section, we aim to investigate the effect of the chosen tracer on the extraction of the cosmic web. In this context, we compare the connectivity estimates from filaments extracted from gas particle distribution to those identified from the mock-galaxy distribution in THE THREE HUNDRED regions.

The simulated cosmic web is traced by the mock-galaxies catalogue of the full $1 h^{-1}$ Gpc MDPL2 box at redshift $z = 0$. Haloes are defined as a mock-galaxy if they have a minimum stellar mass of $M_* \geq 3 \times 10^9 h^{-1} M_{\odot}$, which corresponds to haloes with $M_{halo} > 3 \times 10^{10} h^{-1} M_{\odot}$. The density is computed from the Delaunay tessellation of the points with the DTFE. The tessellation is mass-weighted, with a weight associated with each tessellation vertex corresponding to the mass of the halo at this vertex, to improve the filament identification, as explained in detail by Kuchner et al. (2020). The cosmic web skeleton is then identified with DisPerSE with a persistence threshold of $6.5\sigma^8$, which provides the best agreement with the cosmic web extracted from gas particles, as tested in Kuchner et al. (2020). A more detailed description of the extraction procedure and in-depth analysis of filament properties from the full MDPL2 box will be provided in a dedicated paper (Bianconi et al., in prep).

We associate the DisPerSE nodes to simulated groups, considering as matched those with a distance of less than 4 pixels, as explained in detail in Section 3.2. The final sample, for all the 324 regions, includes 836 galaxy groups and clusters with a mass range of $10^{13} \leq M_{200} h^{-1} M_{\odot} \leq 2.69 \times 10^{15}$. Lastly, we estimate the connectivity k_{200} of the galaxy clusters at R_{200} , as defined in Section 4.

The results of the connectivity k_{200} estimated from mock-galaxies filaments are plotted in Fig. 11 in red, as a function of the cluster's mass M_{200} . We plot as blue dots the connectivity values computed from gas filaments, presented in Section 4.1.

⁸ Here, the persistence threshold is in terms of number of σ of the distribution and it is defined as the ratio – not the difference, as in the persistence cut – of the values of the points in a critical pair.

We performed the same linear fitting as for the gas connectivity, whose parameters are shown in Table 3.

Table 3: The fitting parameters for the $\log k_{200} - \log M_{200}$ relation for gas-traced filaments and mock-galaxy-traced filaments.

Tracer	A	B
Mock-Galaxies	0.291 ± 0.018	-3.66 ± 0.26
Gas	0.308 ± 0.019	-3.86 ± 0.27

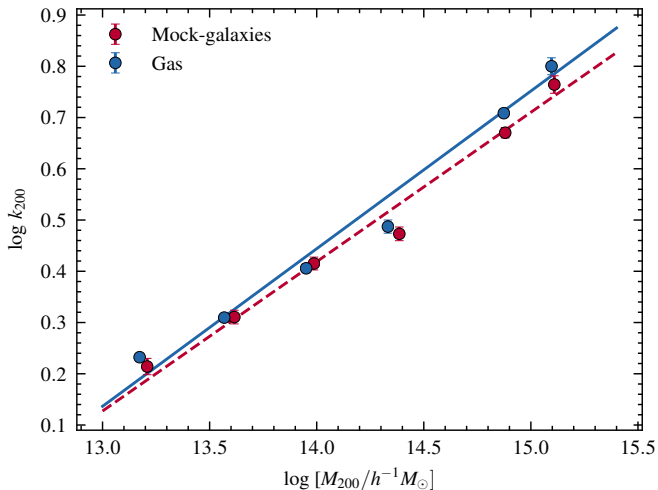


Fig. 11: The mean connectivity of THE THREE HUNDRED groups and clusters at $z = 0$, estimated from gas and mock-galaxies filaments. The mean values of connectivity k_{200} from gas filaments are plotted in blue, the values of k_{200} from mock-galaxies filaments in red. The solid and dashed lines represent the linear fitting, respectively for the gas and the mock-galaxies. The error bars are the errors on the mean values, computed with the bootstrap method.

The strong agreement between the two connectivities is an indication that the number of filaments traced by gas or mock-galaxies is similar and therefore that these are representative of the same structures. However, potential discrepancies between the skeletons extracted from gas or DM particles and haloes catalogues are expected, as noted in other studies (e.g. Bond et al. 2010a,b; Laigle et al. 2018; Kuchner et al. 2020; Zakharova et al. 2023). These discrepancies are likely to be attributed to the finer sampling of the density field by gas particles, which outnumber the mock-galaxies, and therefore could result in reduced noise during the cosmic web extraction process. Moreover, employing different density field estimation methods - a regular grid for the gas particles and the Delaunay tessellation for the mock-galaxies - may introduce some variations in the extracted skeletons, such as a preferred direction for the filamentary structures. The discrepancies between the two tracers and the effects on the recovered cosmic web are investigated more in detail by Bianconi et al. (in prep).

6. Conclusions

The outskirts of galaxy clusters can provide insightful information for the study of large-scale structures. In particular, the presence of filamentary structures, acting as pathways for matter transportation towards the centre of clusters, and their impact

on clusters' properties can be investigated. The aim of this study is to examine the correlation between the connectivity and the main galaxy clusters properties.

In this work, we have used the 324 regions with a $30 h^{-1}$ Mpc side of THE THREE HUNDRED hydrodynamical simulation to extract the filamentary structures around galaxy clusters and groups. We ran the DisPerSE algorithm on the gas particle density maps at redshifts $z = 0, 1$ and 2. The full procedure of generating the density maps has been described together with the setting of relevant parameters of DisPerSE. We have estimated the connectivity at several apertures, in particular at R_{500} , R_{200} and R_{vir} for $\sim 10^3$ groups and clusters with a total mass range of $10^{13} \leq M_{200} h^{-1} M_{\odot} \leq 2.62 \times 10^{15}$ at redshift $z = 0$.

The main results of this work can be summarized as follows:

- (i) The connectivity, computed as the number of gas filaments crossing the sphere at a specific aperture, quantified in terms of overdensity, depends on the chosen radius, with larger values of connectivity when estimated at a larger radius. This is a consequence of including filaments that start from substructures - maxima and bifurcation points - that lie within the radius considered. Therefore, it is important to specify the aperture chosen when analysing the connectivity of galaxy clusters.
- (ii) Filaments have an impact on galaxy cluster mass accretion, transporting matter from the outskirts to the centre. On average, more massive galaxy clusters are also more connected. This result is in agreement with several literature studies, both from observed and simulated data sets.
- (iii) We observe a decrease in the connectivity mean values over cosmic time, with clusters being more connected at higher redshifts. This result is likely to be a consequence of the anisotropic collapse of the cosmic web structures.
- (iv) No dependence of connectivity with the cluster's dynamical state is found. The connectivity-mass correlation does not have any significant difference when computed for three sub-samples of clusters: dynamically relaxed, hybrid and disturbed. Moreover, we do not observe any correlation between the connectivity and the degree of relaxation parameter χ . On the other hand, we find that, independently of the connectivity, more massive clusters are on average more dynamically disturbed.
- (v) No correlation of the hydrostatic mass bias with the redshift is found for the 324 central clusters. This result is independent of the aperture at which the quantities are computed and the observable properties used to infer the hydrostatic mass bias. Moreover, we do not observe a variation in the scatter of the bias with the connectivity, contrary to what is found with the dynamical state of clusters. This suggests that the connectivity may not be an indicator of the dynamical state.
- (vi) We observe a strong agreement between the connectivity evaluated from gas-traced filaments and mock-galaxies-traced filaments, extracted from the mock haloes catalogue of the full MDPL2 box. This result suggests that the gas and mock-galaxies are distinct and complementary tracers of the same structures.

This work underlines the dependence of filaments, traced by the gas particle distribution, on the properties of galaxy clusters to which they are connected and shows a correlation between the connectivity and the total mass of the clusters. This result affirms the role that filaments have in the accretion of matter towards the centre of the cluster.

The results presented in this work and the simulated cosmic web skeletons will be used as a reference for cosmic web

extraction from Compton- γ simulated maps, to provide insightful forecasts for observations. With further investigations on filaments evolution with cosmic time, useful information on the study of cosmology and structure evolution can be provided. Further work is needed to assess the differences in the cosmic web extraction process from distinct tracers and from different density field estimation methods. Future analysis with different hydrodynamical codes, such as the GIZMO-SIMBA run of THE THREE HUNDRED (Cui et al. 2022), will be necessary to investigate the dependence of the results on different baryonic models.

Acknowledgements. This work has been made possible by THE THREE HUNDRED collaboration. The simulations used in this paper have been performed in the MareNostrum Supercomputer at the Barcelona Supercomputing Center, thanks to CPU time granted by the Red Española de Supercomputación. As part of THE THREE HUNDRED project, this work has received financial support from the European Union's Horizon 2020 Research and Innovation programme under the Marie Skłodowska-Curie grant agreement number 734374, the LACEGAL project. S.S. acknowledge support from Sapienza Università di Roma thanks to "Progetti per Avvio alla Ricerca", n. AR123188AF0D68BF, and "Bando Mobilità Internazionale PhD", D.R. n. 1505/2023. M.D.P., S.S. and A.F. acknowledge financial support from PRIN 2022 (Mass and selection biases of galaxy clusters: a multi-probe approach - n. 20228B938N) and from Sapienza Università di Roma, thanks to Progetti di Ricerca Medi 2022, RM1221816758ED4E. G.Y., W.C. and S.S. would like to thank also Ministerio de Ciencia e Innovación (Spain) for financial support under project grant PID2021-122603NB-C21. W.C. is also supported by the Atracción de Talento Contract no. 2020-T1/TIC-19882 granted by the Comunidad de Madrid in Spain, and the science research grants were from the China Manned Space Project.

References

- Alpaslan, M., Robotham, A. S. G., Driver, S., et al. 2014, MNRAS, 438, 177
- Ansarifard, S., Rasia, E., Biffi, V., et al. 2020, A&A, 634, A113
- Aragón-Calvo, M. A., Jones, B. J. T., van de Weygaert, R., & van der Hulst, J. M. 2007, A&A, 474, 315
- Aragón-Calvo, M. A., Platen, E., van de Weygaert, R., & Szalay, A. S. 2010a, ApJ, 723, 364
- Aragón-Calvo, M. A., van de Weygaert, R., & Jones, B. J. T. 2010b, MNRAS, 408, 2163
- Beck, A. M., Murante, G., Arth, A., et al. 2016, MNRAS, 455, 2110
- Bond, J. R., Kofman, L., & Pogosyan, D. 1996, Nature, 380, 603
- Bond, N. A., Strauss, M. A., & Cen, R. 2010a, MNRAS, 406, 1609
- Bond, N. A., Strauss, M. A., & Cen, R. 2010b, MNRAS, 409, 156
- Bonjean, V., Aghanim, N., Salomé, P., Douspis, M., & Beelen, A. 2018, A&A, 609, A49
- Bonnaire, T., Aghanim, N., Decelle, A., & Douspis, M. 2020, A&A, 637, A18
- Boselli, A. & Gavazzi, G. 2006, PASP, 118, 517
- Boselli, A. & Gavazzi, G. 2014, A&ARv, 22, 74
- Bulichi, T.-E., Davé, R., & Kraljic, K. 2024, MNRAS, 529, 2595
- Cadiou, C., Pichon, C., Codis, S., et al. 2020, MNRAS, 496, 4787
- Cautun, M., van de Weygaert, R., & Jones, B. J. T. 2013, MNRAS, 429, 1286
- Cautun, M., van de Weygaert, R., Jones, B. J. T., & Frenk, C. S. 2014, MNRAS, 441, 2923
- Codis, S., Pogosyan, D., & Pichon, C. 2018, MNRAS, 479, 973
- Cohn, J. D. 2022, MNRAS, 513, 624
- Colless, M., Dalton, G., Maddox, S., et al. 2001, MNRAS, 328, 1039
- Cornwell, D. J., Kuchner, U., Gray, M. E., et al. 2024, MNRAS, 527, 23
- Cui, W., Dave, R., Knebe, A., et al. 2022, MNRAS, 514, 977
- Cui, W., Knebe, A., Yepes, G., et al. 2018a, MNRAS, 480, 2898
- Cui, W., Knebe, A., Yepes, G., et al. 2018b, MNRAS, 473, 68
- Cui, W., Power, C., Borgani, S., et al. 2017, MNRAS, 464, 2502
- Danforth, C. W., Keeney, B. A., Tilton, E. M., et al. 2016, ApJ, 817, 111
- Darragh Ford, E., Laigle, C., Gozaliasl, G., et al. 2019, MNRAS, 489, 5695
- Davé, R., Anglés-Alcázar, D., Narayanan, D., et al. 2019, MNRAS, 486, 2827
- Davé, R., Cen, R., Ostriker, J. P., et al. 2001, ApJ, 552, 473
- De Luca, F., De Petris, M., Yepes, G., et al. 2021, MNRAS, 504, 5383
- Donnan, C. T., Tojeiro, R., & Kraljic, K. 2022, NatAs, 6, 599
- Eckert, D., Jauzac, M., Shan, H., et al. 2015, Nature, 528, 105
- Edelsbrunner, Letscher, & Zomorodian. 2002, Discrete & Computational Geometry, 28, 511–533
- Falck, B. L., Neyrinck, M. C., & Szalay, A. S. 2012, ApJ, 754, 126
- Forero-Romero, J. E., Hoffman, Y., Gottlöber, S., Klypin, A., & Yepes, G. 2009, MNRAS, 396, 1815
- Forman, R. 1998, Advances in Mathematics, 134, 90–145
- Galárraga-Espinosa, D., Aghanim, N., Langer, M., Gouin, C., & Malavasi, N. 2020, A&A, 641, A173
- Galárraga-Espinosa, D., Cadiou, C., Gouin, C., et al. 2024, A&A, 684, A63
- Gianfagna, G., Rasia, E., Cui, W., et al. 2023, MNRAS, 518, 4238
- Gouin, C., Bonnaire, T., & Aghanim, N. 2021, A&A, 651, A56
- Gyulassy, A., Bremer, P.-T., Hamann, B., & Pascucci, V. 2008, IEEE Transactions on Visualization and Computer Graphics, 14, 1619–1626
- Haggar, R., Gray, M. E., Pearce, F. R., et al. 2020, MNRAS, 492, 6074
- Hellwing, W. A., Cautun, M., van de Weygaert, R., & Jones, B. T. 2021, PhRvD, 103, 063517
- Hernández-Aguayo, C., Springel, V., Pakmor, R., et al. 2023, MNRAS, 524, 2556
- Hincks, A. D., Radiconi, F., Romero, C., et al. 2022, MNRAS, 510, 3335
- Hoffman, Y., Metuki, O., Yepes, G., et al. 2012, MNRAS, 425, 2049
- Klypin, A., Yepes, G., Gottlöber, S., Prada, F., & Heß, S. 2016, MNRAS, 457, 4340
- Knollmann, S. R. & Knebe, A. 2011, AHF: Amiga's Halo Finder, Astrophysics Source Code Library, record ascl:1102.009
- Kotecha, S., Welker, C., Zhou, Z., et al. 2022, MNRAS, 512, 926
- Kraljic, K., Arnouts, S., Pichon, C., et al. 2018, MNRAS, 474, 547
- Kravtsov, A. V. & Borgani, S. 2012, ARA&A, 50, 353
- Kuchner, U., Aragón-Salamanca, A., Pearce, F. R., et al. 2020, MNRAS, 494, 5473
- Kuchner, U., Aragón-Salamanca, A., Rost, A., et al. 2021, MNRAS, 503, 2065
- Kuchner, U., Haggar, R., Aragón-Salamanca, A., et al. 2022, MNRAS, 510, 581
- Laigle, C., Pichon, C., Arnouts, S., et al. 2018, MNRAS, 474, 5437
- Libeskind, N. I., van de Weygaert, R., Cautun, M., et al. 2018, MNRAS, 473, 1195
- Lokken, M., Cui, W., Bond, J. R., et al. 2023, MNRAS, 523, 1346
- Malavasi, N., Aghanim, N., Douspis, M., Tanimura, H., & Bonjean, V. 2020a, A&A, 642, A19
- Malavasi, N., Aghanim, N., Tanimura, H., Bonjean, V., & Douspis, M. 2020b, A&A, 634, A30
- Malavasi, N., Langer, M., Aghanim, N., Galárraga-Espinosa, D., & Gouin, C. 2022, A&A, 658, A113
- Malavasi, N., Sorce, J. G., Dolag, K., & Aghanim, N. 2023, A&A, 675, A76
- Nelson, D., Springel, V., Pillepich, A., et al. 2019, ComAC, 6, 2
- Nicastro, F., Kaastra, J., Krongold, Y., et al. 2018, Nature, 558, 406
- Peebles, P. J. E. 1980, The large-scale structure of the universe
- Piffaretti, R. & Valdarnini, R. 2008, A&A, 491, 71
- Planck Collaboration XIII. 2016, A&A, 594, A13
- Power, C., Knebe, A., & Knollmann, S. R. 2012, MNRAS, 419, 1576
- Rasia, E., Meneghetti, M., Martino, R., et al. 2012, NJPh, 14, 055018
- Rost, A., Kuchner, U., Welker, C., et al. 2021, MNRAS, 502, 714
- Rost, A. M., Nuza, S. E., Stasyszyn, F., et al. 2024, MNRAS, 527, 1301
- Sarron, F., Adami, C., Durret, F., & Laigle, C. 2019, A&A, 632, A49
- Schaap, W. E. & van de Weygaert, R. 2000, A&A, 363, L29
- Schaye, J., Crain, R. A., Bower, R. G., et al. 2015, MNRAS, 446, 521
- Shull, J. M., Smith, B. D., & Danforth, C. W. 2012, ApJ, 759, 23
- Song, H., Laigle, C., Hwang, H. S., et al. 2021, MNRAS, 501, 4635
- Sousbie, T. 2011, MNRAS, 414, 350
- Sousbie, T., Pichon, C., & Kawahara, H. 2011, MNRAS, 414, 384
- Springel, V. 2005, MNRAS, 364, 1105
- Springel, V. & Hernquist, L. 2003, MNRAS, 339, 312
- Steinborn, L. K., Dolag, K., Hirschmann, M., Prieto, M. A., & Remus, R.-S. 2015, MNRAS, 448, 1504
- Tanimura, H., Aghanim, N., Douspis, M., Beelen, A., & Bonjean, V. 2019, A&A, 625, A67
- Tanimura, H., Aghanim, N., Douspis, M., & Malavasi, N. 2022, A&A, 667, A161
- Tanimura, H., Aghanim, N., Kolodzig, A., Douspis, M., & Malavasi, N. 2020, A&A, 643, L2
- Tempel, E., Stoica, R. S., Kipper, R., & Saar, E. 2016, A&C, 16, 17
- Tornatore, L., Borgani, S., Dolag, K., & Matteucci, F. 2007, MNRAS, 382, 1050
- Tuominen, T., Nevalainen, J., Tempel, E., et al. 2021, A&A, 646, A156
- van de Weygaert, R. & Schaap, W. 2009, The Cosmic Web: Geometric Analysis, ed. V. J. Martínez, E. Saar, E. M. Gonzales, & M. J. Pons-Borderia (Berlin, Heidelberg: Springer Berlin Heidelberg), 291–413
- Vogelsberger, M., Genel, S., Springel, V., et al. 2014, Nature, 509, 177
- Winkel, N., Pasquali, A., Kraljic, K., et al. 2021, MNRAS, 505, 4920
- York, D. G., Adelman, J., Anderson, John E., J., et al. 2000, AJ, 120, 1579
- Zakharova, D., Vulcani, B., De Lucia, G., et al. 2023, MNRAS, 525, 4079
- Zel'dovich, Y. B. 1970, A&A, 5, 84

Appendix A: Connectivity and cluster overdensity at higher redshift

The connectivity depends on the aperture at which it is estimated, independently of the redshift. We plot the mean values of k_{500} , k_{200} and k_{vir} as a function of the cluster mass at redshift $z = 1$ and $z = 2$, respectively in Figs. A.1 and A.2.

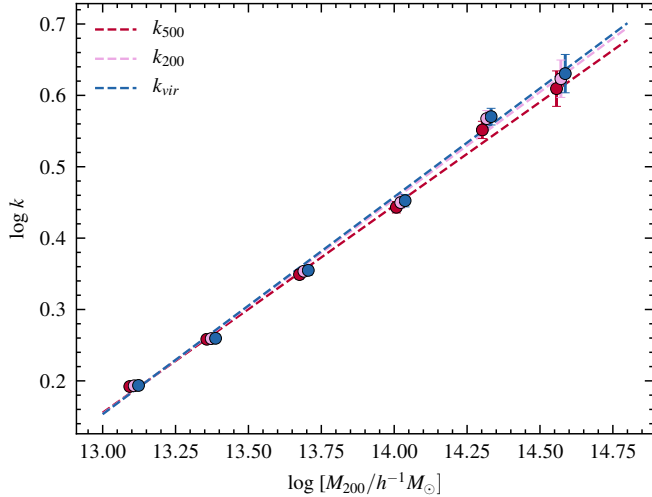


Fig. A.1: The mean connectivity of THE THREE HUNDRED groups and clusters at $z = 1$ as a function of the mass M_{200} . The connectivity is estimated at different over-densities, respectively k_{500} in red, k_{200} in pink and k_{vir} in blue. The dashed lines represent the linear fitting. The error bars are the errors on the mean values, computed with the bootstrap method. The mean values are shifted in mass for visual clarity.

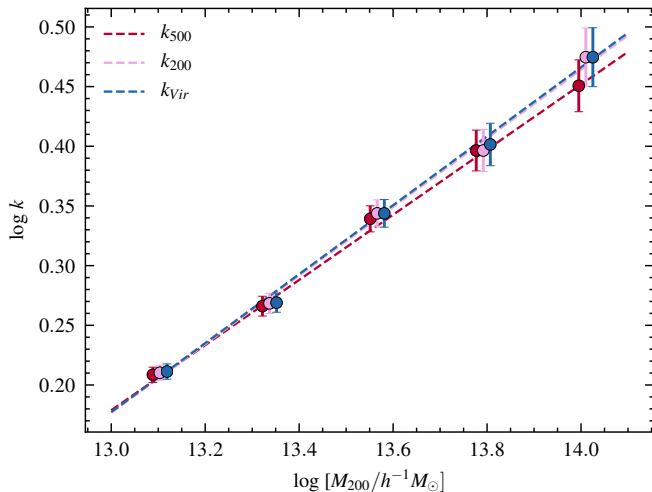


Fig. A.2: The mean connectivity of THE THREE HUNDRED groups and clusters at $z = 2$ as a function of the mass M_{200} . The connectivity is estimated at different over-densities, respectively k_{500} in red, k_{200} in pink and k_{vir} in blue. The dashed lines represent the linear fitting. The error bars are the errors on the mean values, computed with the bootstrap method. The mean values are shifted in mass for visual clarity.

Appendix B: Connectivity and dynamical state at higher redshift

The connectivity and mass correlation is not dependent on the dynamical state of the cluster, regardless of the redshift. We plot in Figs. B.1 and B.2 the connectivity mean values as a function of the mass for dynamically relaxed, hybrid and disturbed clusters, respectively at redshift $z = 1$ and $z = 2$.

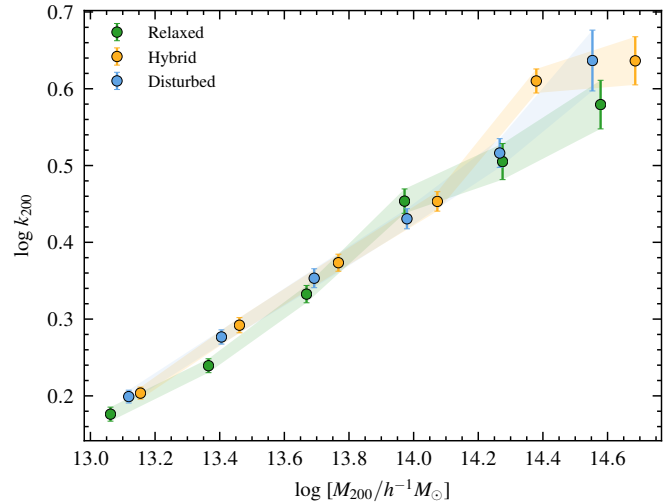


Fig. B.1: Connectivity and mass relation for three dynamical state sub-samples at redshift $z = 1$. In green the connectivity mean values k_{200} for the dynamically relaxed clusters, in yellow for hybrid clusters, and in light blue the values for dynamically disturbed clusters. The error bars represent the errors of the mean, computed with the bootstrap method.

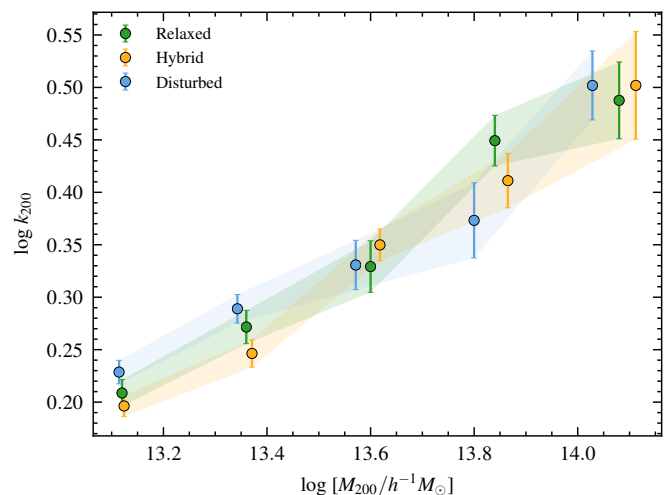


Fig. B.2: Connectivity and mass relation for three dynamical state sub-samples at redshift $z = 2$. In green the connectivity mean values k_{200} for the dynamically relaxed clusters, in yellow for hybrid clusters, and in light blue the values for dynamically disturbed clusters. The error bars represent the errors of the mean, computed with the bootstrap method.

Appendix C: Connectivity and dynamical state at different overdensities

The connectivity and mass correlation is not dependent on the dynamical state of the cluster, independently of the overdensity at which the connectivity and the dynamical state are estimated. We plot in Figs. C.1 and C.2 the connectivity mean values as a function of the mass for dynamically relaxed, hybrid and disturbed clusters, estimated respectively at R_{500} and R_{vir} .

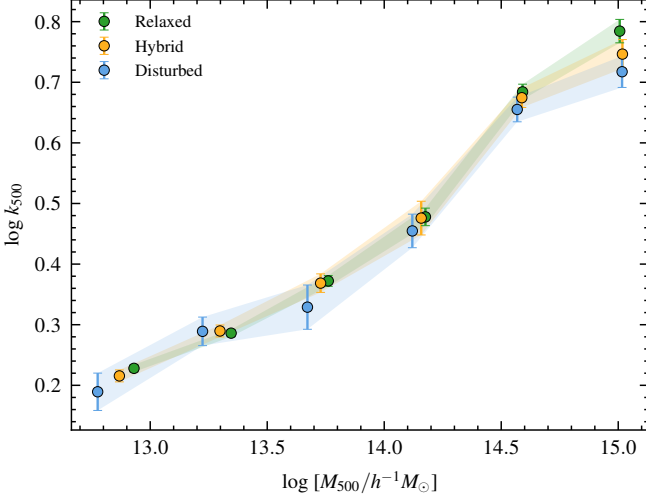


Fig. C.1: Connectivity and mass relation for three dynamical state sub-samples at redshift $z = 0$, estimated at R_{500} . In green the connectivity mean values k_{500} for the dynamically relaxed clusters, in yellow for hybrid clusters, and in light blue the values for dynamically disturbed clusters. The error bars represent the errors of the mean, computed with the bootstrap method.

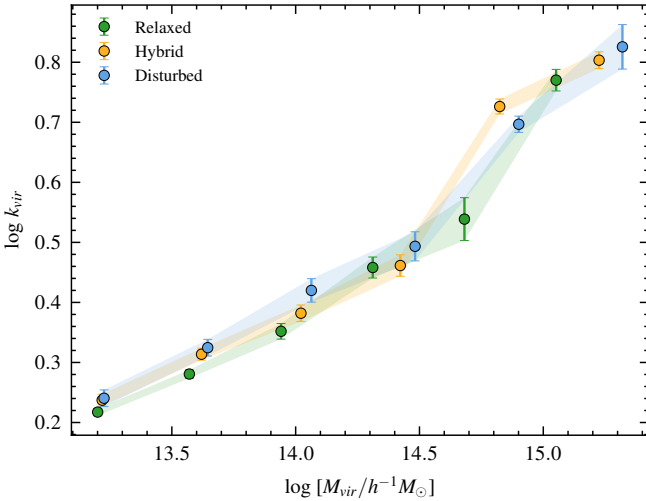


Fig. C.2: Connectivity and mass relation for three dynamical state sub-samples at redshift $z = 0$, estimated at R_{vir} . In green the connectivity mean values k_{vir} for the dynamically relaxed clusters, in yellow for hybrid clusters, and in light blue the values for dynamically disturbed clusters. The error bars represent the errors of the mean, computed with the bootstrap method.

Appendix D: Connectivity and HE bias at R_{500}

We plot in Fig. D.1 the median values of the hydrostatic mass biases b_X , in green, and b_{SZ} , in violet, computed at R_{500} as a function of the connectivity k_{500} . A correlation between the connectivity and the hydrostatic mass bias is not observed.

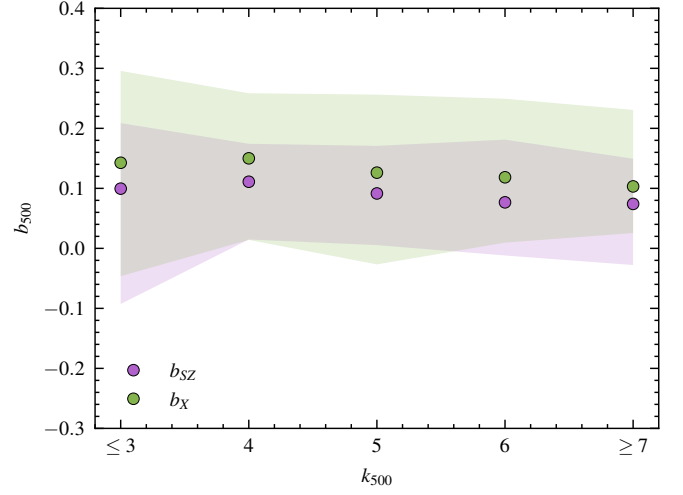


Fig. D.1: Connectivity and hydrostatic mass bias relation at redshift $z = 0$. In green the mass bias median values b_X estimated at R_{500} , in violet the mass bias median values b_{SZ} at R_{500} . The shaded areas represent the 16th and 84th percentiles.